

Data Processing for Short-Term Solar Irradiance Forecasting using Ground-Based Infrared Images

Guillermo Terrén-Serrano*, Manel Martínez-Ramón

*Department of Electrical and Computer Engineering, The University of New Mexico,
Albuquerque, NM 87131, United States.*

Abstract

The generation of energy in a power grid which uses Photovoltaic (PV) systems depends on the projection of shadows from moving clouds in the Troposphere. This investigation proposes an efficient method of data processing for the statistical quantification of cloud features using long-wave infrared (IR) images and Global Solar Irradiance (GSI) measurements. The IR images are obtained using a data acquisition system (DAQ) mounted on a solar tracker. We explain how to remove cyclostationary biases in GSI measurements. Seasonal trends are removed from the GSI time series, using the theoretical GSI to obtain the Clear-Sky Index (CSI) time series. We introduce an atmospheric model to remove from IR images both the effect of atmosphere scatter irradiance and the effect of the Sun's direct irradiance. Scattering is produced by water spots and dust particles on the germanium lens of the enclosure. We explain how to remove the scattering effect produced by the germanium lens attached to the DAQ enclosure window of the IR camera. An atmospheric condition model classifies the sky-conditions in four different categories: clear-sky, cumulus, stratus and nimbus. When an IR image is classified in the category of clear-sky, it is used to model the scattering effect of the germanium lens.

Keywords: Image processing, Machine Learning, Sky Imaging, Long-wave Infrared Camera, Sun-Tracking, Solar Forecasting

1. Introduction

The steadily increasing penetration of renewable energy in the power grid [1], is raising investments in the investigation of solar technologies [2]. As a direct consequence of the research efforts, PV systems are reducing their manufacturing cost and increasing their efficiency [3]. The main advantage of PV

*Corresponding author.

E-mail addresses: guillermoterren@unm.edu (Guillermo Terrén-Serrano), manel@unm.edu (Manel Martínez-Ramón)

systems is their capability of regulating the dispatch of energy when enough solar resource is available [4, 5]. Considering the current state of the grids, power grid operators and policy makers would benefit from pursuing an upgrade in communication systems so that they can incorporate smart technologies [6].

Clouds produce variation on the solar irradiance that reaches the surface of the Earth [7]. In fact, these effects are more severe when produced by cumulus clouds [8]. Clouds may also produce an increase in the solar irradiance that reaches the surface of the Earth when clouds are near the circumsolar area [9]. These effects are a consequence of the scattering produced by the clouds on solar irradiance [10]. In particular, the projection of shadows over PV arrays produced by passing clouds causes drops in the energy generated by large PV plants [11]. To have a reliable supply of solar energy it is necessary to equip a Smart Grid (SG) with solar forecasting algorithms [12, 13, 14].

Forecasting algorithms which predict the power output of a PV system are not extrapolative to other PV systems connected to the same grid [15, 16, 17]. This is because the power output of a PV system depends on different factors such as the configuration of PV arrays and the efficiency of the PV cells [18, 19, 20]. Furthermore, the forecasting of GSI provides a SG with the information necessary to regulate the dispatch of energy from different nearby PV plants. The complexity of a Machine Learning (ML) forecasting algorithm is reduced when cyclostationary components are removed from the analyzed time series [21, 22]. Like GSI, CSI forecasting is extrapolative, while at the same time, reducing the complexity of the algorithm [23, 24].

Meso-scale meteorology and numerical weather prediction models are computationally expensive when the forecasting horizon ranges from 1 to 5 minutes [17, 25, 26]. An alternative to these methods is to forecast CSI using satellite images [27, 28, 29], but the transmission of images from geostationary satellites might have a delay of up to an hour [30]. In the application of very short-term solar irradiance forecasting [31], ground-based methods found that the cloud cover and the direction of the velocity vectors in the circumsolar area are highly correlated with the future solar irradiance [32].

When the Sun appears in a visible light imaging system, the pixels in the circumsolar area are saturated [33, 34, 35, 36]. Near IR filters attached to visible light cameras attenuate the effect of the Sun's direct irradiance [37]. When a fisheye lens is attached to a visible camera, the Field of View (FOV) is enlarged to enable all-sky images [38]. Innovations in ground-based imaging systems increase the feasible FOV of IR images [39]. Ground-based radiometric IR cameras [40], which record thermal images [41, 42], were used to analyze statistical features of clouds [43]. The objective was to classify the cloud's optical depth to find an obstruction free path for optical communication between the Earth and satellites [44]. The stabilization of atmospheric measurements is possible when using thermal imagery from microbolometers [45]. These technologies provide low-cost sky imaging hardware for applications of solar forecasting algorithms [46, 47]. In addition, the use of sky imaging systems mounted on a solar tracker were proven to increase the performance of solar forecasting algorithms [48, 37].

An accurate segmentation of clouds enhances the performance of solar fore-

casting algorithms [49, 50]. The velocity vectors may be used to know the direction and speed of clouds [28]. The velocity vectors are computed using the optical flow equation, which is based in two assumptions. The first assumption is the constant intensity of the objects in two consecutive images [51, 52, 53]. However, the intensity of clouds increases as they approach the circumsolar area in visible light imaging. The second assumption is smooth changes of intensity in the images. Sky images have an intensity gradient when the Sun is in the images. The gradient decreases as a function of the distance of a pixel to the Sun [54]. Velocity vectors computed using a dense implementation of a cross-correlation method [55] are computationally expensive for the application of the very short-term GSI forecasting [56].

Debris such as water stains and dust particles can accumulate on outdoor DAQ systems. This debris can scatter the irradiance and produce artifacts in the images that can appear similar to clouds. The camera window in the enclosure of sky imaging systems requires routine cleaning. DAQ systems are generally installed in areas without easy access [57]. Software can reduce maintenance by removing some of these effects.

This investigation explains how to detrend the seasonal component in GSI measurements to obtain the CSI time series. This is performed optimizing the parameters of the GSI physical model to fit the GSI measurements of a pyranometer. The pyranometer is installed on a horizontal surface near to our sky imaging system. A model that combines atmospheric irradiance scattering and the Sun's direct irradiance in IR sky imaging is introduced for solar forecasting algorithms. The parameters of the atmospheric scattering model depend on the time and the weather conditions. We propose to model the parameters of the atmosphere irradiance scattering model using weather features recorded from a near weather station.

This research introduces an algorithm to model the scattering produced by debris accumulated on the outdoor window of the IR camera. This algorithm uses the last IR images that were detected as having clear-sky conditions. The detection is performed with a classification model that distinguishes between four classes of sky-conditions. To our knowledge, no literature has been published in solar forecasting to explain how to deal with the effects of accumulated debris on an outdoor germanium lens. This problem is common in ground-based sky imaging DAQ systems.

2. Global Solar Irradiance Measurements

To detrend the GSI measurements and obtain the CSI, the cycle-stationary component of pyranometer measurements has to match the theoretical GSI. The GSI is measured in units of W/m^2 . However, the GSI measurements of the pyranometer are biased with respect to the theoretical GSI. In order to model the bias, it is decomposed in two different biases which are the amplitude and the shifting bias. In this section is explained to model these biases independently to detrend the time series of GSI measurements.

2.1. Global Solar Irradiance Physical Model

The theoretical GSI \mathcal{I}_{GSI} calculated in a horizontal surface normal to the ground has three components [58],

$$\mathcal{I}_{GSI} = \mathcal{I}_{Direct} + \mathcal{I}_{Diffuse} + \mathcal{I}_{Reflected}. \quad (1)$$

The direct component of the GSI is a function of the Sun's elevation angle ε ,

$$\mathcal{I}_{Direct} = \mathcal{I}_{DN} \cdot \sin \varepsilon, \quad (2)$$

where the Direct Normal (DN) component is

$$\mathcal{I}_{DN} = \theta_1 \cdot \exp\left(-\frac{\theta_2}{\sin \varepsilon}\right), \quad (3)$$

θ_1 is the surface altitude with respect to the sea level and θ_2 is the air mass coefficient.

The diffuse component of the GSI represents the scattered solar irradiance when hitting particles in the atmosphere such as the water droplets forming clouds. The Diffuse component for a horizontal surface normal to the ground is

$$\mathcal{I}_{Diffuse} = \theta_3 \cdot \frac{\mathcal{I}_{DN}}{2}, \quad (4)$$

where the θ_3 coefficient defines the proportion of irradiance that is scattered for an atmospheric condition.

The reflected component of GSI depends on the tilt angle of the surface. In our problem, the tilt angle is 0° because it is an horizontal surface normal to the ground so the expression is

$$\mathcal{I}_{Reflected} = \theta_4 \cdot \mathcal{I}_{DN} \cdot (\theta_3 + \sin \varepsilon), \quad (5)$$

θ_4 is the reflective coefficient of the ground material where the surface is placed normal to it.

When these three equations are put together, the \mathcal{I}_{GSI} is defined as function of the coefficients set $\boldsymbol{\theta}^1 = \{\theta_1, \dots, \theta_4\} \in \mathbb{R}$ and the Sun elevation angle ε ,

$$\mathcal{I}_{GSI}(\boldsymbol{\theta}^1, \varepsilon) = \mathcal{I}_{DN} \cdot \sin \varepsilon + \theta_3 \cdot \frac{\mathcal{I}_{DN}}{2} + \theta_4 \cdot \mathcal{I}_{DN} \cdot (\theta_3 + \sin \varepsilon), \quad (6)$$

where $\mathcal{I}_{DN} = \theta_1 \cdot \exp(-\theta_2/\sin \varepsilon)$. These three coefficients $\boldsymbol{\theta}^1$ can be calculated from the following a set of theoretical formulæ,

$$\begin{aligned} \theta_1 &= 1160 + 75 \cdot \sin\left(\frac{360}{N} \cdot (d - 275)\right), \\ \theta_2 &= 0.174 + 0.035 \cdot \sin\left(\frac{360}{N} \cdot (d - 27)\right), \\ \theta_3 &= 0.095 + 0.4 \cdot \sin\left(\frac{360}{N} \cdot (d - 27)\right), \end{aligned} \quad (7)$$

where are in function of the day of the year d and the number of days in a year N [58]. The coefficient θ_4 amounts for the reflected irradiance. As the pyranometer is mounted on a black surface, the $\mathcal{I}_{Reflected}$ is assumed negligible so $\theta_4 = 0$.

2.1.1. Physical Model Optimization

To detrend the measurements from the pyranometer and obtain the CSI, the set of parameters $\boldsymbol{\theta}^1$ of the theoretical GSI in Eq. (6) is optimized to fit the GSI measurements of the pyranometer. The time series of GSI measurements from the pyranometer are defined as $\mathbf{y}_d = \{y_{d,k} \in \mathbb{R}^+ \mid k = 1, \dots, K_d\}$, and their corresponding elevation angles are $\boldsymbol{\varepsilon}_d = \{\varepsilon_{d,k} \in [0, \frac{\pi}{2}] \mid k = 1, \dots, K_d\}$. K_d is the number of samples in day d . There are $d = \{d \in \mathbb{N}^{[1,N]} \mid d = 1, \dots, D\}$ days of clear-sky GSI measurements. The following numerical optimization problem is solved for each day to find the optimal set of a parameters $\hat{\boldsymbol{\theta}}_d^1$,

$$\hat{\boldsymbol{\theta}}_d^1 = \underset{\boldsymbol{\theta}_d^1}{\operatorname{argmin}} \mathcal{E}(\boldsymbol{\theta}_d^1), \quad \forall d = 1, \dots, D. \quad (8)$$

The optimal set of parameters are those that minimized the error function $\mathcal{E}(\cdot)$ that is defined as

$$\mathcal{E}(\boldsymbol{\theta}_d^1) = \frac{1}{K_d} \sum_{k=1}^{K_d} \sqrt{(y_{d,k} - \mathcal{I}_{GSI}(\boldsymbol{\theta}_d^1, \varepsilon_{d,k}))^2}, \quad (9)$$

this function is the Root Mean Square Error (RMSE).

The gradient of the RMSE function w.r.t of each parameter $\theta_{d,i}^1$ in the set $\boldsymbol{\theta}^1$ is computed for each day d ,

$$\frac{\partial \mathcal{E}(\boldsymbol{\theta}_d^1)}{\partial \theta_{d,i}^1} = -\frac{1}{K_d} \sum_{k=1}^{K_d} \left[\frac{y_{d,k} - \mathcal{I}_{GSI}(\boldsymbol{\theta}_d^1, \varepsilon_{d,k})}{|y_{d,k} - \mathcal{I}_{GSI}(\boldsymbol{\theta}_d^1, \varepsilon_{d,k})|} \cdot \frac{\partial \mathcal{I}_{GSI}(\boldsymbol{\theta}_d^1, \varepsilon_{d,k})}{\partial \theta_{d,i}^1} \right]. \quad (10)$$

and an optimal set of parameters $\hat{\boldsymbol{\theta}}_d^1$ is obtained for each day d .

2.2. Pyranometer Amplitude Bias

The amplitude of the GSI measurements from the pyranometer is attenuated by a bias σ_d which is different in each day d . The amplitude bias σ_d is calculated with the theoretical GSI evaluated using the coefficients $\hat{\boldsymbol{\theta}}_d^1$ obtained in Eq. (10) and the coefficient $\boldsymbol{\theta}_d^1$ obtained in Eq. (7),

$$\sigma_d = \frac{\max [\mathcal{I}_{GSI}(\hat{\boldsymbol{\theta}}_d^1, \boldsymbol{\varepsilon}_d)]}{\max [\mathcal{I}_{GSI}(\boldsymbol{\theta}_d^1, \boldsymbol{\varepsilon}_d)]}, \quad \forall d = 1, \dots, D, \quad \sigma_d \in \mathbb{R}^{[1,2]}. \quad (11)$$

The amplitude bias σ_d follows a periodic function with the frequency of a year. This parameter is modelled using a cycle-stationary sinusoidal function,

$$\mathcal{C}(\boldsymbol{\theta}^2, d) = \theta_1 \cdot \sin\left(\theta_2 + \frac{2\pi d}{N}\right) + \theta_3, \quad (12)$$

where N is the days in a year, d is the day of the year, and $\boldsymbol{\theta}^2 = \{\theta_1, \theta_2, \theta_3\} \in \mathbb{R}$ is the set of parameters. The optimal set of parameters $\boldsymbol{\theta}^2$ are computed minimizing the error function,

$$\hat{\boldsymbol{\theta}}^2 = \underset{\boldsymbol{\theta}^2}{\operatorname{argmin}} \mathcal{E}(\boldsymbol{\theta}^2), \quad (13)$$

where error function $\mathcal{E}(\cdot)$ is the RMSE defined as,

$$\mathcal{E}(\boldsymbol{\theta}^2) = \frac{1}{D} \cdot \sum_{d=1}^D \sqrt{(\sigma_d - \mathcal{C}(\boldsymbol{\theta}^2, d))^2}. \quad (14)$$

The error function is minimized using numerical optimization. The gradient w.r.t. $\boldsymbol{\theta}^2$,

$$\frac{\partial \mathcal{E}(\boldsymbol{\theta}^2)}{\partial \theta_i^2} = -\frac{1}{D} \sum_{d=1}^D \left[\frac{\sigma_d - \mathcal{C}(\boldsymbol{\theta}^2, d)}{|\sigma_d - \mathcal{C}(\boldsymbol{\theta}^2, d)|} \frac{\partial \mathcal{C}(\boldsymbol{\theta}^2, d)}{\partial \theta_i^2} \right]. \quad (15)$$

The amplitude bias in the measurements is corrected as,

$$\hat{y}_{d,k} = \frac{y_{d,k}}{\sigma_d}, \quad \hat{y}_{d,k} \in \mathbb{R}^+, \quad (16)$$

where $\sigma_d \triangleq \mathcal{C}(\boldsymbol{\theta}^2, d)$ and $y_{d,k}$ is the GSI measure-sample k in day d .

2.3. Pyranometer Shifting Bias

The theoretical GSI is defined as $i_{d,k} \triangleq \mathcal{I}_{GSI}(\boldsymbol{\theta}_d^1, \varepsilon_{d,k})$, and the corrected GSI measurements from the pyranometer is $\hat{y}_{d,k}$. To correct the shifting in the measurement, the correlation between is computed to find where is the maximum,

$$\hat{k}_d = \underset{k_d}{\operatorname{argmax}} \mathbf{Corr}(\mathbf{i}_d[k], \hat{\mathbf{y}}_d[k]), \quad \forall d = 1, \dots, D, \quad (17)$$

where \hat{k}_d is the maximum correlation sample of day d , so $\Delta k_d = [k_{d,N/2}] - \hat{k}_d$ is the displacement of the time series and $\mathbf{sign}(\Delta k_d)$ is the direction of the displacement.

The theoretical GSI \mathbf{i}_d is shifted to detrend the measurements from the pyranometer $\hat{\mathbf{y}}_d$ using the displacement from the maximum Δk_d ,

$$\mathbf{y}_d \triangleq \begin{cases} \frac{\hat{\mathbf{y}}_{d, [\Delta k_d: K_d]}}{\mathbf{i}_{d, [1: K_d - \Delta k_d]}} & \mathbf{sign}(\Delta k_d) = 1 \\ \frac{\hat{\mathbf{y}}_{d, [1: K_d - \Delta k_d]}}{\mathbf{i}_{d, [\Delta k_d: K_d]}} & \mathbf{sign}(\Delta k_d) = -1 \end{cases} \quad \forall k = 1, \dots, K_d - \Delta k_d, \quad (18)$$

where \mathbf{y}_d is the CSI. When the CSI time series \mathbf{y}_d is multiplied by the theoretical GSI time series without shifting, the corrected measurements $\hat{\mathbf{y}}'_d$ are obtained,

$$\hat{\mathbf{y}}'_d = \begin{cases} \mathbf{y}_d \cdot \mathbf{i}_{d, [\Delta k_d: K_d]} & \mathbf{sign}(\Delta k_d) = 1 \\ \mathbf{y}_d \cdot \mathbf{i}_{d, [1: K_d - \Delta k_d]} & \mathbf{sign}(\Delta k_d) = -1 \end{cases} \quad \forall k = 1, \dots, K_d - \Delta k_d. \quad (19)$$

There is information loss using this method for the correction. The corrected time series $\hat{\mathbf{y}}'_d$ is Δk_d samples shorter. However, this does not suppose a problem as it is only used information from samples where $\varepsilon > 18^\circ$.

The model proposed to approximate the shiftings in the GSI measurements from pyranometer is a piece-wise model. The set of models in the piece-wise model $\mathcal{PW}(\boldsymbol{\theta}^3, \boldsymbol{\delta}, d)$ are defined as straight lines without slop. There are four different models. The parameters $\boldsymbol{\theta}^3$ indicates a shifting depending on the day of the year of the sample. Domain of the models are defined as $\boldsymbol{\delta} = \{\delta_1, \delta_2, \delta_3, \delta_4, \delta_5, \delta_6\}$ and shiftings are $\boldsymbol{\theta}^3 = \{\theta_1^3, \theta_2^3, \theta_3^3, \theta_4^3, 0\}$. The piece-wise model is defined as,

$$\mathcal{PW}(\boldsymbol{\theta}^3, \boldsymbol{\delta}, d) = \begin{cases} \theta_1^3 & \delta_1 \leq d < \delta_2 \\ \theta_2^3 & \delta_2 \leq d < \delta_3 \\ \theta_3^3 & \delta_3 \leq d < \delta_4 \\ \theta_4^3 & \delta_4 \leq d < \delta_5 \\ \theta_5^3 & \delta_5 \leq d \leq \delta_6 \end{cases} \quad \forall d = 1, \dots, D, \quad (20)$$

the optimal shifting in each domain is approximated as the sample mean,

$$\hat{\theta}_i^3 = \frac{1}{|\delta_i \leq d < \delta_{i+1}|} \sum_{d \in \delta_i \leq d < \delta_{i+1}} \Delta k_d, \quad \forall i = 1, \dots, 4, \quad (21)$$

where $|\cdot|$ denotes the cardinality of the training samples in the set.

2.4. Steepest Descent Algorithm

We propose to estimate the optimal set of parameters $\hat{\boldsymbol{\theta}}^1$ and $\hat{\boldsymbol{\theta}}^2$ using Steepest Descent method for numerical optimization [59]. The algorithm begins with the random initialization of each parameter in $\boldsymbol{\theta}^1$ or $\boldsymbol{\theta}^2$, so that $\theta_i^{(0)} \sim \mathcal{U}(0, K_i)$ where K_i is the maximum feasible value of parameter θ_i . The set of parameters is iteratively updated following a formula of function gradient that i,

$$\theta_i^{(t+1)} = \theta_i^{(t)} - \eta \cdot \frac{\partial \mathcal{E}(\boldsymbol{\theta}^{(t)})}{\partial \theta_i^{(t)}}, \quad (22)$$

where $\eta \in \mathbb{R}^+$ is a very small number. Therefore, there is a series of parameters set updates that converges to a function minima. The optimization algorithm stops when $\mathcal{E}(\boldsymbol{\theta}^{(t+1)}) \geq \mathcal{E}(\boldsymbol{\theta}^{(t)})$ and the optimal set is $\hat{\boldsymbol{\theta}} \triangleq \boldsymbol{\theta}^{(t)}$. The algorithm is randomly initialized N times so,

$$\hat{\boldsymbol{\theta}} = \underset{\boldsymbol{\theta}}{\operatorname{argmin}} \left\{ \mathcal{E}(\hat{\boldsymbol{\theta}}_1), \dots, \mathcal{E}(\hat{\boldsymbol{\theta}}_N) \right\}. \quad (23)$$

3. Infrared Radiometric Images

The measurements from the radiometric IR camera are temperatures in centikelvin degrees. The raw intensities in an IR image of a sample k are defined

as $\mathbf{I}^k = \{I_{i,j}^k \in \mathbb{R}^+ \mid \forall i = 1, \dots, M, \forall j = 1, \dots, N\}$. The temperatures are obtained from the raw intensities,

$$T_{i,j}^k = \frac{I_{i,j}^k}{100} [K] \quad (24)$$

in the international system units, or

$$T_{i,j}^k = \frac{I_{i,j}^k}{100} - 273.15 [C] \quad (25)$$

in Celsius degrees.

3.1. Atmospheric Irradiance Model

The methods to estimate the motion vectors in an image are sensitive to the intensity gradient. Therefore, it is necessary to remove the gradient produced by the solar direct irradiance and the atmospheric scatter irradiance in order to extract dynamic features from the cloud. The diffuse or scatter irradiance are emitted by water molecules or dust particles in the atmosphere. The scatter irradiance from the atmosphere dome has systematical pattern that appear on the IR images in the course of a year.

3.1.1. Solar Irradiance Models

The Sun direct irradiance is scattered by aerosol and water particles floating in the atmosphere [60]. The scatter irradiance depends on the atmosphere air mass and clearness conditions. The air mass varies with the altitude, because the gravity attracts particles concentrating them near the surfaces. The clearness depends on the weather conditions such as wind that disperse the aerosol particles.

The aim is to remove the scatter and direct irradiance from the IR images, so that only the irradiance from clouds appears on the images. Each pixel in a frame is defined as a point $\mathbf{x} = \{x, y\}$ in a Cartesian coordinates system, so that $\mathbf{X} = \{(1, \dots, N) \mid x, \in \mathbb{N}, i = 1, \dots, M, j = 1, \dots, N\}$ and $\mathbf{Y} = \{(1, \dots, M) \mid y_{i,j} \in \mathbb{N}, i = 1, \dots, M, j = 1, \dots, N\}$. The functions proposed to model the effect from the background atmospheric irradiance is an exponential function,

$$\mathcal{S}(y_{i,j}; y_0, \sigma_1, \lambda_1) = \sigma_1 \exp\left(\frac{y_{i,j} - y_0}{\lambda_1}\right), \quad \sigma_1, \lambda_1 \in \mathbb{R}, \quad (26)$$

where σ_1 is the scale and λ_1 is the length-scale. The function is centered in the Sun which pair of coordinates is $\mathbf{x}_0 = \{x_0, y_0\}$.

The effect produced by the direct irradiance from the Sun on the IR image is modeled by a bivariate quadratic exponential function centered in \mathbf{x}_0 . The Cauchy distribution, which is inverse-quadratic bivariate function, with length-scale parameter λ_2 is more flexible in the height and tails. The multivariate

Cauchy distribution function is

$$\mathbf{Ca}(\mathbf{x}_{i,j}; \mathbf{x}_0, \lambda_2) = \frac{1}{2\pi} \cdot \left\{ \frac{\lambda_2}{\left[(x_{i,j} - x_0)^2 + (y_{i,j} - y_0)^2 + \lambda_2^2 \right]^{\frac{3}{2}}} \right\}, \quad \lambda_2 \in \mathbb{R}. \quad (27)$$

The Cauchy distribution is transformed to a Lorentzian function multiplying it by a scale parameter σ_2 that controls the density height. The Lorentzian function is

$$\mathcal{D}(\mathbf{x}_{i,j}; \mathbf{x}_0, \sigma_2, \lambda_2) = \sigma_2 \left\{ \frac{\lambda_2^2}{\left[(x_{i,j} - x_0)^2 + (y_{i,j} - y_0)^2 + \lambda_2^2 \right]^{\frac{3}{2}}} \right\}, \quad \sigma_2, \lambda_2 \in \mathbb{R}. \quad (28)$$

This function is not a probability distribution, as its integral does not add to 1, but we do not intent to modeling probabilities so this is not important for us.

Combining the functions for the scatter irradiance $\mathcal{S}(\cdot)$ and the direct irradiance from the Sun $\mathcal{D}(\cdot)$, the function of atmospheric background $\mathcal{A}(\cdot)$ is obtained,

$$\begin{aligned} \mathcal{A}(\mathbf{x}_{i,j}; \mathbf{x}_0, \boldsymbol{\theta}) &= \theta_1 \exp \left\{ \frac{y_{i,j} - y_0}{\theta_2} \right\} \\ &+ \theta_3 \left\{ \frac{\theta_4^2}{\left[(x_{i,j} - x_0)^2 + (y_{i,j} - y_0)^2 + \theta_4^2 \right]^{\frac{3}{2}}} \right\}, \end{aligned} \quad (29)$$

which set of parameters is $\boldsymbol{\theta} = \{\sigma_1, \lambda_1, \sigma_2, \lambda_2\}$. This function is used to model the deterministic component of the irradiance in the IR images.

3.1.2. Optimal Parameters

The atmospheric model has to be fit in all the sample-frames. We found that the parameters of the atmospheric irradiance model are variables of a function that depends on the weather conditions, the date, and the Sun's position in the horizon. The fit of the model is not necessary is a model of the parameters is available. To approximate the function that models the parameters, the optimal parameters are found in previously recorded frames during different days of year with clear-sky conditions so that only the irradiance appears on the IR images. The raw intensity of the pixels is defined as $\mathbf{I}^{d,k}$ for sample k in day d . The RMSE function of the sample k in day d is,

$$\mathcal{E}(\boldsymbol{\theta}^{d,k}) = \frac{1}{MN} \cdot \sum_{i=1}^M \sum_{j=1}^N \sqrt{\left(i_{i,j}^{d,k} - \mathcal{A}(\mathbf{x}_{i,j}; \mathbf{x}_0^{d,k}, \boldsymbol{\theta}^{d,k}) \right)^2}. \quad (30)$$

The objective is to find the optimal set of parameters $\boldsymbol{\theta}^{d,k}$ that minimizes the loss function for sample k in day d ,

$$\hat{\boldsymbol{\theta}}^{d,k} = \underset{\boldsymbol{\theta}^{d,k}}{\operatorname{argmin}} \mathcal{E}(\boldsymbol{\theta}^{d,k}), \quad \forall k = 1, \dots, K_d, \quad \forall d = 1, \dots, D. \quad (31)$$

The gradient of error function $\mathcal{E}(\boldsymbol{\theta}^{d,k})$ w.r.t. the parameters $\theta_i^{d,k}$ for a sample k in day d is,

$$\frac{\partial \mathcal{E}(\boldsymbol{\theta}^{d,k})}{\partial \theta_i^{d,k}} = -\frac{1}{MN} \sum_{j=1}^{MN} \left[\frac{\tilde{z}_j^{d,k} - \mathcal{A}(\tilde{\mathbf{x}}_j; \mathbf{x}_0^{d,k}, \boldsymbol{\theta}^{d,k})}{|\tilde{z}_j^{d,k} - \mathcal{A}(\tilde{\mathbf{x}}_j; \mathbf{x}_0^{d,k}, \boldsymbol{\theta}^{d,k})|} \frac{\partial \mathcal{A}(\tilde{\mathbf{x}}_j; \mathbf{x}_0^{d,k}, \boldsymbol{\theta}^{d,k})}{\partial \theta_i^{d,k}} \right], \quad (32)$$

where $\tilde{\mathbf{i}}^{d,k} = \mathbf{vec}(\mathbf{I}^{d,k})$, $\tilde{\mathbf{y}} = \mathbf{vec}(\mathbf{Y})$, and $\tilde{\mathbf{x}} = \mathbf{vec}(\mathbf{X})$ for notation simplification.

3.1.3. Model of the Parameters

Once the optimal set of parameters $\hat{\boldsymbol{\theta}}^{d,k}$ are found for each sample k in a day d , the aim is to model the optimal sets of parameters $\hat{\boldsymbol{\theta}} = \{\hat{\boldsymbol{\theta}}_k \in \mathbb{R}^4 \mid \forall k = 1, \dots, D \cdot K_d\}$ for any possible time of a year. The set of parameters has a physical interpretation. The parameter θ_1 is the average height of the Tropopause in the IR image. This height varies along the year as a function of the latitude and the weather conditions. The parameter θ_2 models the cycle-stationary pattern of the Earth curvature cross-section. The great circle of Tropopause is not perfectly spherical because of the prospective. The height of the Tropopause is influenced by global climatic patterns.

The parameter θ_1 and θ_2 are modelled using the Sun's position which is defined by the azimuth $\boldsymbol{\alpha} = \{\alpha_k \in \mathbb{R}^{[1, 2\pi]} \mid \forall k = 1, \dots, D \cdot K_d\}$ and the elevation angle $\boldsymbol{\varepsilon} = \{\varepsilon_k \in \mathbb{R}^{[1, \frac{\pi}{2}]} \mid \forall k = 1, \dots, D \cdot K_d\}$. The samples are from a set of days $\mathbf{d} = \{d_k \in \mathbb{N}^{[1, 365]} \mid \forall k = 1, \dots, D \cdot K_d\}$. The height of the Tropopause is approximated by ground measurements of air temperature $\mathbf{T}^{air} = \{T_k^{air} \in \mathbb{R} \mid \forall k = 1, \dots, D \cdot K_d\}$ and dew point $\mathbf{T}^{dew} = \{T_k^{dew} \in \mathbb{R} \mid \forall k = 1, \dots, D \cdot K_d\}$. The feature vectors are defined as \mathbf{x}_k^1 for θ_1 and \mathbf{x}_k^2 for θ_2 . The features in the vectors are $\mathbf{x}_k^1 = \{T_k^{air}, T_k^{dew}, \varepsilon_k, \alpha_k\}$ and $\mathbf{x}_k^2 = \{d_k, \varepsilon_k, \alpha_k\}$ for any frame k .

The coefficients \mathbf{w}^i are fitted to a polynomial expansion of order n of the feature vectors $\mathcal{P}(\mathbf{x}_k^i)^n$. The polynomial expansion formula applied to the features in vector \mathbf{x}_k^1 is,

$$\mathcal{P}(\mathbf{x}_k^1) = \sum_{j,l,m,p}^P w_{j,l,m,p}^1 \cdot (T_k^{air})^j \cdot (T_k^{dew})^l \cdot (\varepsilon_k)^m \cdot (\alpha_k)^p, \quad \forall k = 1, \dots, D \cdot K_d. \quad (33)$$

The polynomial expansion formula applied to the features in vector \mathbf{x}_k^2 is,

$$\mathcal{P}(\mathbf{x}_k^2) = \sum_{j,l,m}^P w_{j,l,m}^2 \cdot (d_k)^j \cdot (\varepsilon_k)^l \cdot (\alpha_k)^m, \quad \forall k = 1, \dots, D \cdot K_d, \quad (34)$$

The formulation of our regression problem with a loss function applied to the polynomial expansion coefficients, is a simplification of the Tikhonov's regularization [61]. This model when is implemented with the L-2 norm is known as Ridge Regression (RR). The error function is,

$$\min_{\mathbf{w}} \sum_{k=1}^{DK_d} [\mathbf{y}_k - \mathcal{P}(\mathbf{x}_k^i)]^2 + \lambda \cdot \|\mathbf{w}^i\|_2, \quad \forall k = 1, \dots, K_d \cdot D. \quad (35)$$

The parameters \mathbf{w} that minimize the error function are found analytically,

$$\begin{aligned} 0 &= \frac{\partial}{\partial \mathbf{w}} \cdot \left[(\mathbf{y}_k - \mathbf{w}^\top \Phi)^\top (\mathbf{y}_k - \mathbf{w}^\top \Phi) + \lambda \cdot \text{tr}(\mathbf{w}^\top \mathbf{w}) \right] \\ 0 &= 2 \cdot [\Phi^\top (\Phi \mathbf{w} - \mathbf{y}_k) + \lambda \mathbf{w}] \\ \bar{\mathbf{w}} &= (\Phi^\top \Phi + \lambda \cdot \mathbf{I})^{-1} \Phi^\top \mathbf{y}. \end{aligned} \quad (36)$$

The polynomial transformation of the features vectors is $\varphi : \mathcal{X} \mapsto \mathcal{P}^n$, where n is the order of the polynomial expansion. The number of terms in the polynomial expansion is $\mathcal{P}^n = [(n + (d - 1))!]/[n!(d - 1)]$. When applying the transformation to a feature vector such as $\mathbf{x}_k \mapsto \varphi(\mathbf{x}_k)$, $\forall k \in (0, K]$, the resultant vector is transformed to a space of higher dimensions $\varphi(\mathbf{x}_k) \in \mathbb{R}^{\mathcal{P}^n}$. The feature vectors \mathbf{x}_k^1 or \mathbf{x}_k^2 have a scalar dependent variable that is either θ_k^1 or θ_k^2 .

The definition of the problem in matrix form contains the all training samples. The set of matrices for each model \mathcal{M}^i are,

$$\mathbf{y}^i = \begin{bmatrix} \theta_1^i \\ \vdots \\ \theta_K^i \end{bmatrix}, \quad \Phi^i = \begin{bmatrix} \varphi(\mathbf{x}_1^i)_1 & \dots & \varphi(\mathbf{x}_1^i)_{\mathcal{P}^n} \\ \vdots & \ddots & \vdots \\ \varphi(\mathbf{x}_K^i)_1 & \dots & \varphi(\mathbf{x}_K^i)_{\mathcal{P}^n} \end{bmatrix}, \quad \mathbf{w}^i = \begin{bmatrix} w_1^i \\ \vdots \\ w_{\mathcal{P}^n}^i \end{bmatrix}. \quad (37)$$

The prediction of parameter $\hat{\theta}_*^i$ for a new observation \mathbf{x}_*^i is computed independently using each models parameters such as,

$$\hat{\theta}_*^i = (\bar{\mathbf{w}}^i)^\top \varphi(\mathbf{x}_*^i). \quad (38)$$

The parameters of the Sun direct irradiance θ_3 and θ_4 are considered constant as the Sun's irradiance does not varies along the day in the IR images. The optimal value is computed as the sample mean,

$$\hat{\theta} = \frac{1}{D \cdot K_d} \sum_{d=1}^D \sum_{k=1}^{K_d} \theta^{d,k}. \quad (39)$$

The atmospheric irradiance can be approximated for a new observation \mathbf{x}_* , knowing the set of parameters $\hat{\theta}_* = \{\hat{\theta}_1, \dots, \hat{\theta}_4\}$ and the Sun's position is \mathbf{x}_0 , with the model $\hat{\mathbf{I}}_* = \mathcal{A}(\mathbf{X}, \mathbf{Y}; \mathbf{x}_0^k, \hat{\theta}_*)$, where $\hat{\mathbf{I}}_* \in \mathbb{R}^{[1, 2^{16}]}$. When a sequence

of images is defined as space-time the atmospheric model for scatter and direct irradiance is the deterministic component of the solar irradiance,

$$\hat{\mathbf{I}}^k = \left\{ \mathcal{A}(\mathbf{X}, \mathbf{Y}; \mathbf{x}_0^k, \hat{\boldsymbol{\theta}}_k) : k \in [1, \infty) \right\} \in \mathbb{R}^{[1, 2^{16}]}. \quad (40)$$

The implementation of this model is proposed to detrend the 2D-dimensional time series. The image series contains only information from the irradiance emitted by the clouds.

3.1.4. Atmospheric Model Application

The Sun has always constant intensity τ_0 in the images unless a cloud is occluding it, so that the direct irradiance is removed only when it is on the images. If the Sun is detected on the image, the atmospheric irradiance model $\mathcal{A}(\mathbf{X}, \mathbf{Y}; \mathbf{x}_0, \boldsymbol{\theta}_*)$ is applied, otherwise the scatter irradiance model $\mathcal{S}(\mathbf{Y}; y_0, \boldsymbol{\theta}_*)$ is applied,

$$\bar{\mathbf{I}}^k = \begin{cases} \mathbf{I}^k - \mathcal{S}(\mathbf{Y}; y_0, \boldsymbol{\theta}_*) & \max(\mathbf{I}^k) < \tau_0 \\ \mathbf{I}^k - \mathcal{A}(\mathbf{X}, \mathbf{Y}; \mathbf{x}_0, \boldsymbol{\theta}_*) & \text{Otherwise} \end{cases} \quad \bar{\mathbf{I}}^k \in \mathbb{R}. \quad (41)$$

When the model $\mathcal{A}(\mathbf{X}, \mathbf{Y}; \mathbf{x}_0, \boldsymbol{\theta}_*)$ is subtracted to the frames can be errors. The inaccuracies are due to the low resolution of the IR sensor, plus any other systematic errors added by the tracking system.

The intensity of the pixels at distance $\leq r_0$ from the Sun $\mathbf{x}_0 = \{x_0, y_0\}$ is interpolated to attenuate the effect of errors. The nearest neighbors interpolation method is performed using the remaining pixels in the image which are $\mathbf{x} = \{(x_{i,j}, y_{i,j}) \in \mathbb{N} \mid i = 1, \dots, M, j = 1, \dots, r_{i,j} > r_0\}$. A pixel nearest neighbors is,

$$\begin{aligned} \hat{x}_{i,j} &= \operatorname{argmin} |\mathbf{x} - x_{i,j}|, \\ \hat{y}_{i,j} &= \operatorname{argmin} |\mathbf{y} - y_{i,j}|, \quad \forall i, j \in \mathbb{N}^{x_{i,j} \wedge y_{i,j} \leq r_0}. \end{aligned} \quad (42)$$

The intensity of the nearest neighbour is assigned to the pixels in the circumsolar area defined as $x_{i,j} \wedge y_{i,j} \leq r_0$ [62],

$$\bar{\mathbf{I}}^k(x_{i,j}, y_{i,j}) = \bar{\mathbf{I}}^k(\hat{x}_{i,j}, \hat{y}_{i,j}), \quad \forall i, j \in \mathbb{N}^{x_{i,j} \wedge y_{i,j} \leq r_0}, \quad (43)$$

where $r_0 = 3$ is the radius of the circumsolar area.

After removing the direct and scatter atmospheric irradiance, the scattering irradiance emitted by clouds, streetlights or building structures still appears in the IR images. The scatter irradiance emitted by particles attached to the exterior of camera window is also on the IR images. The camera window is made out of germanium. Germanium is a material that allows the transmission of the IR irradiance.

3.2. Germanium Infrared Camera Window Model

The window of the camera gets dirty with water stains produced by dried droplets containing dust particles after rainy days. Dust particles suspended in the air accumulate on the camera window over time. The window cannot be routinely cleaned because of difficult access to the DAQ localization. A persistent model is proposed to remove the effects produced by the dust particles and water spots on the camera window.

3.2.1. Atmospheric Condition Model

The aim is to classify the sky-conditions in four possible categories: clear-sky, cumulus, stratus, or nimbus cloud. The classification determines when an image can be used in the window model. This model may also detect when the sky IR images require segmentation. When cumulus clouds are on the IR images segmentation is required, it is not necessary when thin stratus or thick nimbus clouds cover the all-sky shown in the IR image.

The temperature differences are normalized to 8 bits, $\bar{\mathbf{I}}^k = \{\bar{i}_{i,j}^k \in \mathbb{N}^{2^8} \mid \forall i = 1, \dots, M, \forall j = 1, \dots, N\}$. The lowest value is set to 0 and then divided by the clouds' maximum feasible temperature. The velocity vectors were computed applying the Lucas-Kanade method LK [63, 64]. For each two consecutive images $\bar{\mathbf{I}}^{k-1}, \bar{\mathbf{I}}^k$ of the data set, the velocity vectors are defined as $\mathbf{V}^k = \{\mathbf{v}_{i,j} = (u, v)_{i,j}^k \in \mathbb{R}^2 \mid \forall i = 1, \dots, M, \forall j = 1, \dots, N\}$. The upper index k denoting the frame in the collection of samples K_d of day d is changed in the rest of the document. Instead the under index k is used to denote a sample i in the collection of samples from all the days $N = K_d \cdot D$.

The feature vector includes the atmospheric pressure $\mathbf{p}^{atm} = \{p_k^{atm} \in \mathbb{R} \mid \forall k = 1, \dots, N\}$, the CSI $\mathbf{i}^{csi} = \{i_k^{csi} \in \mathbb{R} \mid \forall k = 1, \dots, N\}$ and a set of statistics. These statistics are: the mean $\mathbb{E}(\cdot)$, the variance $\mathbb{V}(\cdot)$, the kurtosis $\mathbb{K}(\cdot)$ and the skewness $\mathbb{S}(\cdot)$. The statistics were computed using the raw radiometric measurements of temperatures from the IR image \mathbf{T}_k and the magnitude of the velocity vectors $\mathbf{M}_k^2 = \mathbf{U}_k^2 + \mathbf{V}_k^2$. The set of features \mathbf{x}_k in a sample k are

$$\mathbf{x}_i = \{p_k^{atm}, i_k^{csi}, \mathbb{E}(\mathbf{T}_k), \mathbb{V}(\mathbf{T}_k), \mathbb{S}(\mathbf{T}_k), \mathbb{K}(\mathbf{T}_k), \dots, \mathbb{E}(\mathbf{M}_k), \mathbb{V}(\mathbf{M}_k), \mathbb{S}(\mathbf{M}_k), \mathbb{K}(\mathbf{M}_k)\}. \quad (44)$$

A polynomial expansion is applied to the feature vectors such as $\mathbf{x}_k \rightarrow \varphi(\mathbf{x}_k) \in \mathbb{R}^{\mathcal{P}^n}$, where n is the polynomial expansion of order. The atmospheric condition classes are such as $L = \{1, \dots, 4\}$. The dataset in matrix form is,

$$\mathbf{X} = \begin{bmatrix} \varphi(\mathbf{x}_1) \\ \vdots \\ \varphi(\mathbf{x}_N) \end{bmatrix}, \quad \mathbf{X} \in \mathbb{R}^{N \times \mathcal{P}^n}, \quad \mathbf{y} = \begin{bmatrix} y_1 \\ \vdots \\ y_N \end{bmatrix}, \quad \mathbf{y} \in L. \quad (45)$$

A linear Support Vector for Classification (SVC) is proposed to solve the classification problem due to the large number of samples [65, 66]. The formulation of the optimization problem for a dataset $\mathcal{D} = \{\mathbf{X}, \mathbf{y}\}$, where $\mathbf{X} =$

$\{\mathbf{x}_i \in \mathbb{R}^D \mid \forall i = 1, \dots, N\}$ and $\mathbf{y} = \{y_i \in [-1, +1] \mid \forall i = 1, \dots, N\}$, is

$$\min_{\mathbf{w}} \frac{1}{2} \|\mathbf{w}\| + C \sum_{i=1}^N \xi(\mathbf{w}; \mathbf{x}_i, y_i), \quad (46)$$

where $C > 0$ is the penalty term, and $\xi(\mathbf{w}; \mathbf{x}_i, y_i)$ is the loss function that in our model is the L-2 for a SVC, so we have this,

$$\min_{\mathbf{w}} \frac{1}{2} \|\mathbf{w}\|_2 + C \sum_{i=1}^N (\max[0, 1 - y_i \mathbf{w}^\top \mathbf{x}_i])^2. \quad (47)$$

The standard solution of a linear SVC has two possible categories. However, our problem is a multi-class classification problem. The one-versus-all scheme is proposed to implement a multi-class linear SVC. The sets of labels for each one of the linear SVC are defined as,

$$\tilde{\mathbf{y}}_{i,\ell} = \begin{cases} +1 & y_i = \ell \\ -1 & \text{Otherwise} \end{cases} \quad \forall i = 1, \dots, N, \quad \forall \ell \in L. \quad (48)$$

where L is the set of feasible classes in the problem. For a new sample \mathbf{x}_* , its class is obtained such as,

$$\hat{y}_* = \operatorname{argmax}_{\ell \in L} \mathbf{sign}(\mathbf{w}_\ell^\top \mathbf{x}_*), \quad (49)$$

the bias is included in the weights.

If the accuracy of the classification model is not perfect, there will be miss-classifications. The transition between sky-conditions classes is assumed to be slow, so a persistent classification is proposed to attenuate errors due to sporadic artifacts,

$$\hat{\mathbf{y}}_k = [\hat{y}_k \ \cdots \ \hat{y}_{k-t}], \quad (50)$$

where t is the lag in the persistent time series of consecutive classifications. A frame k is classified finding the most persistent class in $\hat{\mathbf{y}}_k$,

$$\hat{y}'_k = \mathbf{mode}(\hat{\mathbf{y}}_k). \quad (51)$$

The persistent vector of sky-conditions classes does not contain the modes \hat{y}'_k , the vector is updated with the output of the model classification \hat{y}_k .

3.2.2. Persistent Infrared Camera Window Model

As the tracking system rotates the particles accumulated on the surface of the window stay constant over short periods of time and consequently is possible to model them. For that, the set \mathcal{I}_k is defined to have up to M selected IR images for each sample k . The IR images $\bar{\mathbf{I}}_k$ were classified as clear-sky images and had

applied the atmospheric model. Therefore, the IR images have only the scatter irradiance produced by artifacts on the germanium window,

$$\mathcal{I}_k = \{\bar{\mathbf{I}}_1, \dots, \bar{\mathbf{I}}_M\}, \quad \bar{\mathbf{I}}_k \in \mathbb{R}^{D \times N}. \quad (52)$$

The vector \mathbf{i}_k is defined as the sequence of the last t CSI measurements,

$$\mathbf{i}_k = [i_k \ \dots \ i_{k-t}], \quad i_k \in \mathbb{R}^+. \quad (53)$$

The average value of the absolute drop in CSI r_k in a sequence of t measurements of i_k is computed as,

$$r_k = \frac{1}{\ell} \sum_{i=0}^{\ell} |1 - i_{k-i}|, \quad r_k \in \mathbb{R}^+, \quad (54)$$

this value is large when the Sun is totally or partially occluded. In fact, the average amount of CSI r_k is also an indicator of when there is not a large cloud such a stratus or a nimbus.

To add robustness to atmospheric conditions classification, a new frame is added to the set iff the classification y_k is clear-sky and the drop on the CSI r_k was under a threshold,

$$\mathcal{I}_k = \begin{cases} \mathcal{I}_k \cup \bar{\mathbf{I}}_k & y_k = 1 \wedge r_k \leq 0.05 \\ \mathcal{I}_k \cap \bar{\mathbf{I}}_k & \text{Otherwise,} \end{cases} \quad (55)$$

where $y_k = 1$ and $r_k \leq 0.05$ is the robustness condition that is always fulfill. The camera window model is updated when there are enough frames M with clear-sky conditions to compute the median image,

$$\mathbf{W}_k = \mathbf{median}(\mathcal{I}_k), \quad \text{iff } |\mathcal{I}_k| \geq M, \quad \mathbf{W}_k \in \mathbb{R}^{D \times N} \quad (56)$$

where $|\cdot|$ the cardinality of the set. The algorithm randomly selects M elements in the set using an uniform sampling to initialize the set that will be used in the next day.

3.2.3. Window Model Application

The window model is applied to an IR image after the subtraction of atmospheric model. This is done to avoid any window artifacts that can affect the quality of the cloud segmentation,

$$\bar{\mathbf{I}}'_k = \bar{\mathbf{I}}_k - \mathbf{W}_k, \quad \bar{\mathbf{I}}_k \in \mathbb{R}^{D \times N}, \quad (57)$$

the obtained image are temperatures increments with respect to the Tropopause.

The fact of having the cloud's intensity in the same interval facilitates the segmentation, and thereby the clouds labelling. To normalize an infrared image of 16 bits to 8 bits is necessary to consider that the average distance from the sea level to the Tropopause is $\sim 12 \text{ km}$ at 36° latitude north [67], but Albuquerque

is at 1,641 *km* above the sea level. Then, if the air temperature decreases by $9.8^\circ/\text{km}$ [68], the maximum feasible intensity that a cloud can have, should be at around: $9,8 \cdot (11,5 - 1,6) \cdot 100 = 9,7 \times 10^3$. The interval where the clouds are recognizable in the images $\bar{\mathbf{I}}'_k$ is,

$$\tilde{\mathbf{I}}_k = \frac{\bar{\mathbf{I}}'_k - \mathbf{min}(\bar{\mathbf{I}}'_k)}{9,7 \times 10^3} \cdot 2^8, \quad \tilde{\mathbf{I}}_k \in \mathbb{N}^{[1,2^8]}. \quad (58)$$

The minimum intensity $\mathbf{min}(\bar{\mathbf{I}}'_k)$ can vary between consecutive images, and it can have a value either above zero (this is most in cloudy condition) or below zero. It is a offset or a floating point in the signal cause by the noise introduced in errors of the atmospheric and window models. Nevertheless, as the normalization is only for segmentation purposes, not for feature extraction, this is not an issue.

4. Experiments

The proposed data processing methods are applied to data acquired by an innovative system, which captures circumsolar IR images at the same time that measures GSI using a pyranometer [56]. The DAQ is equipped with a solar tracker that updates its pan, and tilt every second, maintaining the Sun in a central position in the images along a day. The IR sensor is a Lepton¹ camera with radiometry which has a wavelength from 8 to 14 micros, and provides an uniform thermal image as the output. When the radiometry functionality is enabled, the pixels in a frame are turned into temperature measurements in centikelvin units. The resolution of an IR image is 80×60 pixels. The DAQ is localized on the roof area of UNM-ME building in Albuquerque, NM.

The weather features that were used to remove cyclostationary artifacts on the IR images are: atmospheric pressure, air temperature, dew point and humidity. The weather station is set to measure every 10 minutes, so the data was interpolated to match the IR images sampling interval. The weather station is located at the University of New Mexico Hospital, and both its real-time and historical data are publicly accessible².

4.1. Global Solar Irradiance Measurements Biases Models

The amplitude bias model $\mathcal{C}(\boldsymbol{\theta}^2, d)$ and the shifting bias model $\mathcal{PW}(\boldsymbol{\theta}^3, \boldsymbol{\delta}, d)$ were trained using 54 days of clear-sky. The 30 % of the samples were left aside for testing purpose. The models were cross-validated implementing Leave-One-Out (LOO) method. The amplitude biases are approximated using the periodic model in Eq. (12). The amplitudes bias samples σ_d are calculated with Eq. (11). The shifting are approximated using the piece-wise model in Eq. (20). The piece-wise model has 5 constant levels $\boldsymbol{\theta}^3$ that are computed as the mean

¹<https://www.flir.com/>

²<https://www.wunderground.com/dashboard/pws/KNMALBUQ473>

of the shifts at the level in Eq. (21). The shifting samples Δk_d are computed using Eq. (17). The set of domains is defined as $\delta = \{1, 72, 220, 305, 340, 365\}$ the set of shifting levels θ^3 is cross-validated.

The models were trained leaving one sample out for validation. The parameters of the models were optimized for each training subset of the LOO. The parameters were randomly initialized and optimized using steepest descent method. The optimization was repeated for 5 different initialization of the parameters. The selected set of parameters is the one that achieved smaller RMSE. The cross-validated optimal sets of parameters is the average of all the optimal parameters computed in each iteration of LOO cross-validation (CV) method.

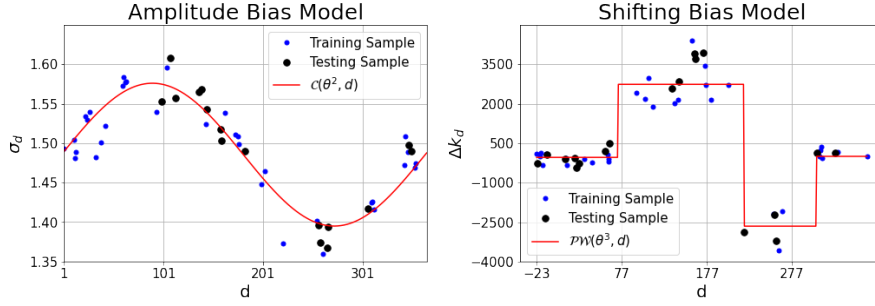


Fig. 1. The graph on the left show estimation of the amplitude σ_d for each day d a year in red color using the model $\mathcal{C}(\hat{\theta}^2, d)$. The samples in blue are the training samples. The ones in black are the testing samples. The graph on the right shows the shifting estimations using piece-wise model $\mathcal{PW}(\hat{\theta}^3, \delta, d)$ is in red. The training samples are in blue color and the testing samples are in black.

4.2. Atmospheric Irradiance Parameters Model

The optimal parameters were found for a dataset consisting of 51 clear-sky conditions days selected out of a year long of samples. The 51 days have no interruptions in the samples. The number of samples available in each day is different since the number of day-light hours in each day are also different. The days were selected from dataset that contains a year set of weather features and IR image samples. 20% of those days were left aside for testing purposes, whilst the remaining of the days were used for training.

LOO-CV method was implemented to find the optimal regularization parameter λ in Eq. (35). The LOO-CV routine was independently implemented for the θ_1 and θ_2 models as the optimal feature vectors are different for each one of the parameter. A sample set was left aside for validation purposes and the remaining were used for training the model. A sample set is a whole day d that has K_d recorded weather features and IR images. The best regularization for a model is the one that obtained the lowest RMSE.

Other variables such as relative humidity or atmospheric pressure, were available but no correlation was found with θ_1 or θ_2 , consequently no further experimentation was carried out with them.

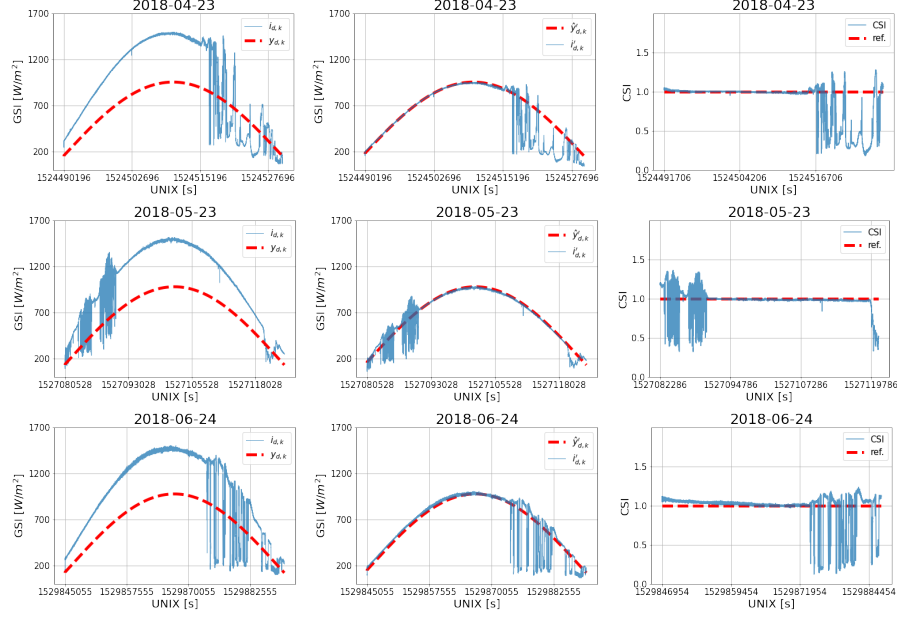


Fig. 2. The graphs on the left column shows the GSI measurements from the pyranometer (blue) and the GSI computed using the theoretical coefficients (red). The graphs on the middle column show the GSI measurements (blue) after correcting the σ_d and Δk_d biases. The graphs in the right show the CSI (blue) obtained detrending the GSI measurements using the theoretical GSI. The reference of the CSI for clear-sky is shown in red.

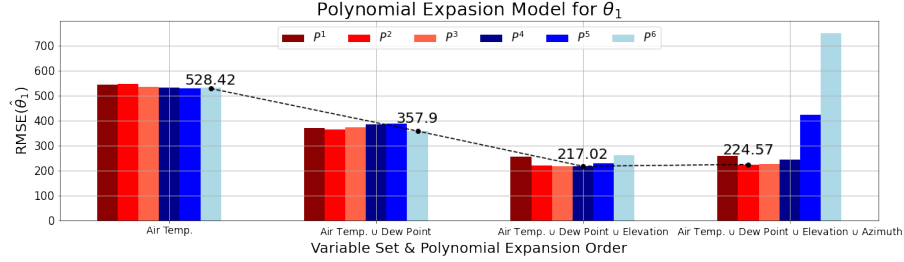


Fig. 3. This graph shows the RMSE in test achieved by the models of θ_1 . The models are grouped by the features included in the vectors. In the models in a group are organized by increasing order of the polynomial expansion from left to right.

4.3. Atmospheric Sky-Conditions Model

The aim in the experiments is to find the polynomial expansion order n and the combination of weather features that produces the highest accuracy in the sky-condition classification. LOO-CV method is implemented to find the optimal complexity C in Eq. (47). The classification accuracy in validation is used to compare linear SVC models with different C .

Consecutive sequences of IR images were manually labelled. The sequences

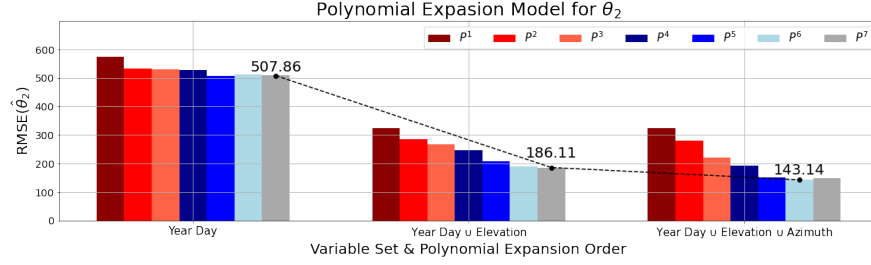


Fig. 4. This graph shows the RMSE in test achieved by the models of θ_2 . The models are grouped by the features included in the vectors. The models in a group are organized by increasing order of the polynomial expansion from left to right.

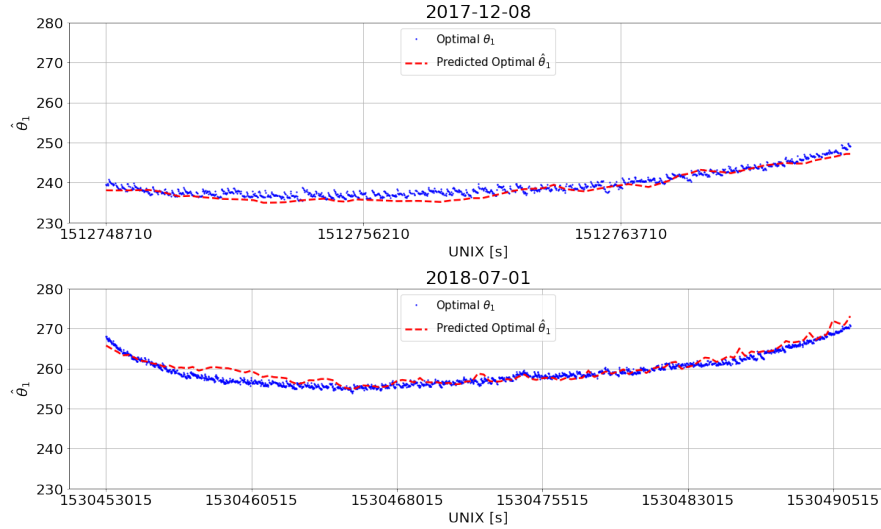


Fig. 5. The graphs show the results of the optimization of the parameter θ_1 in two different days. The days are from the testing subset. The optimal parameters $\theta_1^{d,k}$ computed for each image k are in color blue. The predicted optimal parameters $\hat{\theta}_1^{d,k}$ by the best θ_1 model is in color red.

are from nonconsecutive 21 days. They were randomly selected among the most suitable for training. The IR images have different sky-condition. The sequences were divided into batches with 410 samples. There are 61 batches in total, 41 were used for training and 20 were used for testing. The samples were not scrambled to preserve the time structure in the sequences. The most suitable samples were found to be samples after rainy days. The pattern in the scattering of irradiance produced by dust particles and water stains in enclosure window changes when rains.

When histogram counts are used in the feature vectors instead of the statistics of pixels, the models were found to under-perform and consequently dis-

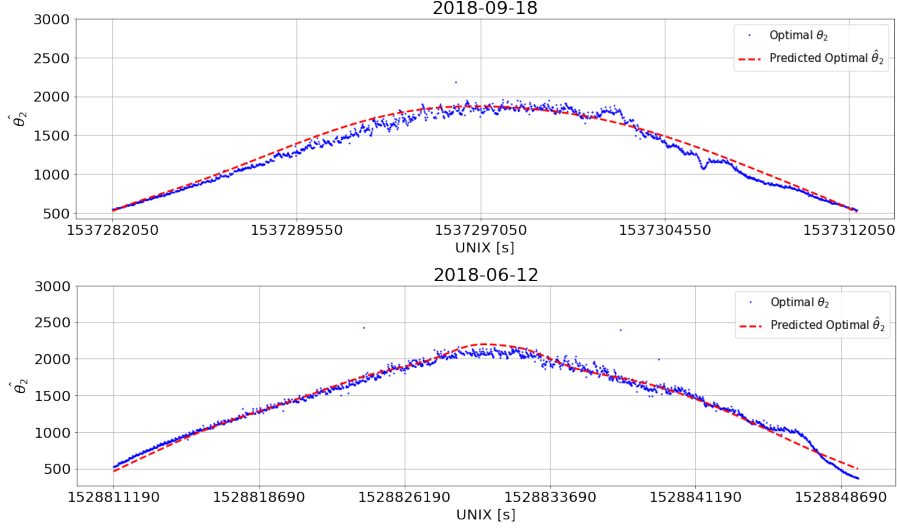


Fig. 6. The graphs show the optimal θ_2 parameters in two clear-sky days of the testing subset. The optimal parameters $\theta_2^{d,k}$ computed for image k are in color blue. The predicted optimal parameters $\hat{\theta}_2^{d,k}$ by the best θ_2 model is in color red.

carded from further experiments. The weather station features that were found to be uncorrelated with the sky-condition classification are: air temperature, dew point, relative humidity, the Sun's elevation and azimuth angles.

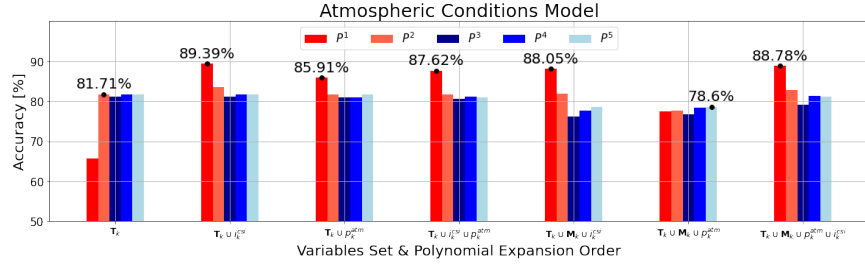


Fig. 7. The graph shows the testing classification accuracy obtained by the sky-condition models. The models are grouped by the features included in the vectors. In the models in a group are organized by increasing order of the polynomial expansion from left to right.

The experiments were carried out in the Wheeler high performances computer of UNM-CARC, which uses SGI AltixXE Xeon X5550 at 2.67GHz with 6 GB of RAM memory per core, has 8 cores per node, 304 nodes total, and runs at 25 theoretical peak FLOPS. It has installed Linux CentOS 7.

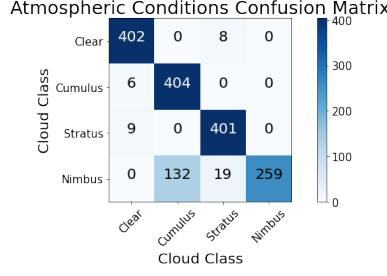


Fig. 8. The graph shows the confusion matrix achieved by the best sky-condition classification model. The best model included the feature vector the statistics of the temperatures and CSI $\mathbf{T}_k \cup \mathbf{z}_k^{csi}$. No polynomial expansion was applied to the features vector.

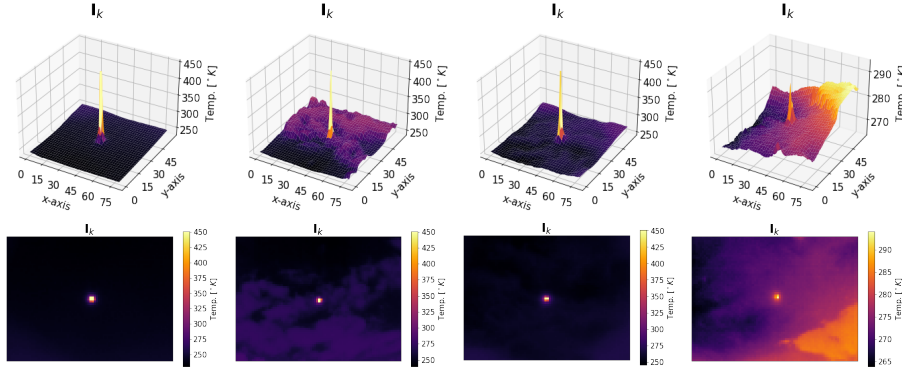


Fig. 9. The graphs in each column corresponds to an IR image from a different day of the year. The IR images were classified by the sky-conditions model as: clear-sky, cumulus cloud, stratus cloud and nimbus cloud. The respective radiometric temperatures images are shown in 3-dimension graphs and in color-scale images.

5. Discussion

The amplitude model testing error is $\text{RMSE}(\hat{\theta}^2) = 0.02$ and the shifting piece-wise model testing error $\text{RMSE}(\hat{\theta}^3) = 440.29$. The fit of models are in Fig. 1. The CSI obtained after detreing the GSI pyranometer measurements using the amplitude and the shifting model are in Fig. 2.

The atmospheric model is composed by the direct and scatter irradiance model. The parameters of direct irradiance model are constant. The parameters of the scatter irradiance model $\hat{\theta}_1$ and $\hat{\theta}_2$ are variables that are modelled as function of weather features. The model of $\hat{\theta}_1$ that obtained the lowest error $\text{RMSE}(\hat{\theta}_1) = 217.02$ (see Fig. 3) uses the air temperature, dew point and the Sun's elevation angle. The feature vector had applied a polynomial expansion of order $n = 4$. The lowest error in test is $\text{RMSE}(\hat{\theta}_2) = 143.14$ in the model of the parameter $\hat{\theta}_1$. The features vectors had applied a polynomial expansion of order $n = 6$. The optimal features were day of the year, the Sun's elevation and azimuth angles (see in Fig. 4). The predict $\hat{\theta}_1$ and $\hat{\theta}_2$ by the best models are in

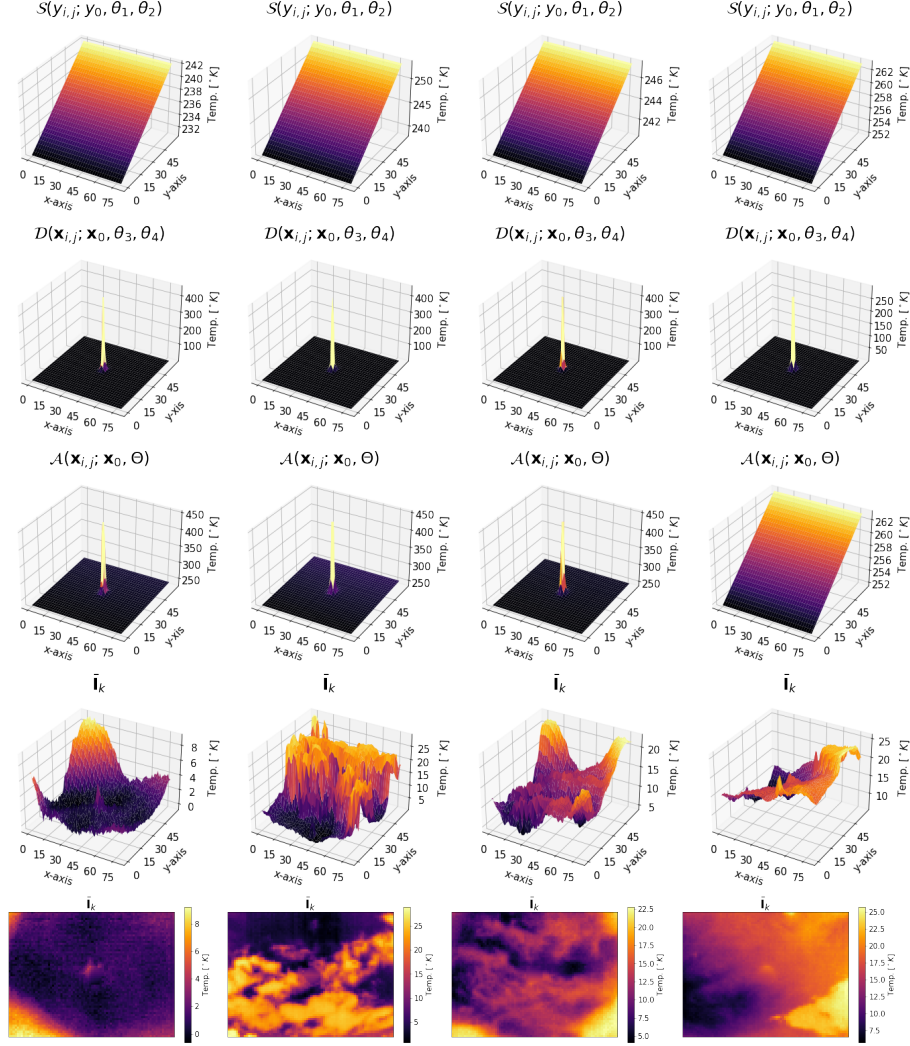


Fig. 10. In the graphs on the upper row show the irradiance scattering model $S(\mathbf{Y}; y_0, \hat{\theta}_1, \hat{\theta}_2)$. The graphs in the middle row show the direct irradiance model $D(\mathbf{X}, \mathbf{Y}; \mathbf{x}_0, \theta_3, \theta_4)$. The graphs in the bottom row shows the atmospheric model $A(\mathbf{X}, \mathbf{Y}; \mathbf{x}_0, \hat{\theta}_3, \hat{\theta}_4)$. Each column shows the models for a different IR image. The color-scale applied to the z-axis is different in each graph. The graphs in last two rows show the incremental temperatures obtained after removing the atmospheric irradiance model from the radiometric temperature images in 3-dimension graph and in color-scale images.

in Fig. 5 and Fig. 6. The figures shows 4 different days in the testing set.

The best SVC model for the classification of the sky-conditions achieved an accuracy of the 89.39% in testing. The optimal feature vector included the statistics of the raw radiometric temperatures from the IR images and CSI. The

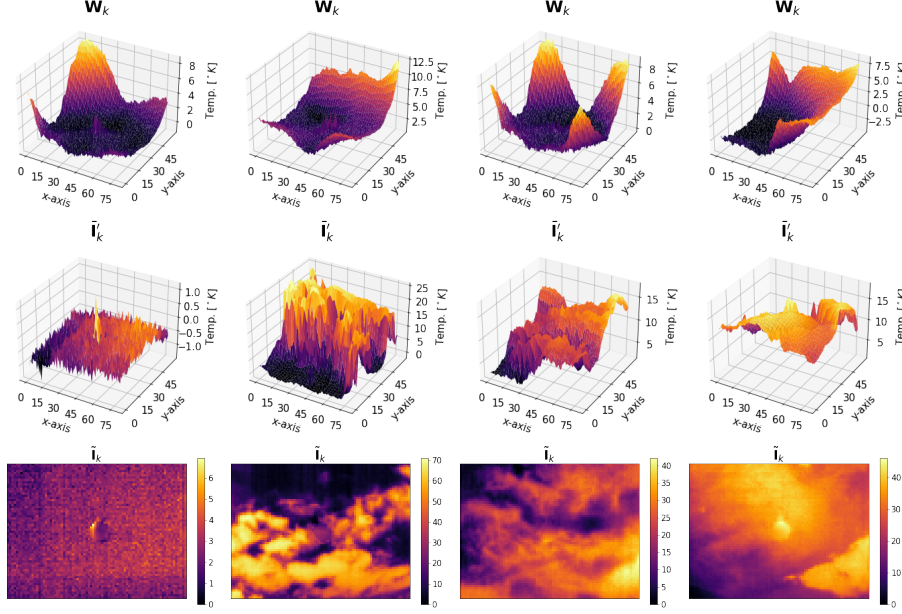


Fig. 11. The graphs in the first row show the window effect in the radiometric measurements of temperature performed by the IR camera. The graphs in the second row show the increments temperatures with respect to the Tropopause temperature in the IR image after removing the effect of the exterior camera window. The images in the third row show the normalized increments of temperatures.

models that include the atmospheric pressure and the statistics of the velocity vectors' magnitude showed poorer performance in the testing subset (see in Fig. 7). The feature vector performed better without applying a polynomial expansion to them. The confusion matrix in test of the best model is shown in Fig. 8. The classification model has an accuracy of 94.69% in clear-sky and 91.97% in stratus cloud conditions. The model has a high rate of miss-classifications when sky-conditions are cumulus or nimbus clouds; the accuracy is 74.54% and 63.17% respectively. However, the accuracy of detecting a sky-condition with any cloud is 98.14%. This is because the cumulus and nimbus clouds appear at lower altitudes than stratus clouds, so they have similar temperatures. The DAQ system captures a small portion of the sky when the Sun's elevation angle is large. The portion of the sky recorded by IR camera may not have enough information to know the size of the clouds. The clear-sky set of IR images in Eq. (52) requires $M \approx 250$ frames to learn the artifacts on the window in Eq. (56). The advantage of using IR cameras instead of visible light camera is that the algorithm can be executed during the night.

The algorithm introduced in this research explains a method to remove the deterministic components of the solar irradiance that appear in an IR sky imaging. For that, an IR image is classified by its sky-condition. The raw radiometric temperatures of four testing images are shown in Fig. 9. These images

were classified as: clear-sky, cumulus cloud, stratus clouds and nimbus cloud. The parameters of the scatter irradiance model were predicted to estimate the atmospheric model for each one of the IR images. The effect caused by atmospheric irradiance were removed from the IR images. The images obtained show the temperature increments with respect to the Tropopause (see results in Fig. 10). The model of the germanium window was estimated using the median image of the last images in the clear-sky set. The effect of the germanium is removed and the temperatures increments are normalized to the feasible range of a cloud (see in Fig. 11).

The radiometric IR cameras have low resolution which is important to understand the complex dynamics of moving clouds. The method of image processing proposed in this research is based in weather features which are obtained from a near weather station. Unfortunately, the sampling interval of near public weather station is low in comparison to the sampling required in an algorithm for very short-term forecasting of solar irradiance.

6. Conclusion

This investigation introduces an efficient data processing method to remove the deterministic component in the solar irradiance which appears in the GSI measurements and IR images. The proper processing of data will reduce the complexity of learning algorithms implemented in the application of solar forecasting. The reduction of the complexity is useful to increase the accuracy of the prediction and to reduce the required computing time to make a prediction. This is of special importance in real-time applications such as very short-term forecasting of solar energy.

The advantage of using radiometric IR technology is that outperform visible light sky imaging in applications with poor light conditions. In addition, the effects of debris can be modelled and remove from the images. An efficient image possessing is necessary when the velocity vectors are computed using the optical flow equation. Otherwise, the computed velocity vectors will bias by the intensity gradients on the images. In situations when the light conditions are adequate for both technologies, IR images are preferable to analyze physical processes such as cloud and solar irradiance. Because thermal images facilitates the extraction of physical features which are suitable to model the underlying physical processes.

The future researches may focus in the development of a atmospheric and window model for visible sky imaging. The acquisition of weather features from a in-situ weather station with the same sampling interval of pyranometer in the DAQ system will increase the performances of the image processing algorithm. The determination of the FOV necessary in a sky imaging system in relation to the forecasting horizon for solar irradiance forecasting algorithm. It would be also interesting to compare the performances of IR versus visible light imaging systems.

7. Acknowledgments

This work has been supported by NSF EPSCoR grant number OIA-1757207 and the King Felipe VI endowed Chair. Authors would like to thank the UNM Center for Advanced Research Computing, supported in part by the National Science Foundation, for providing the high performance computing and large-scale storage resources used in this work.

References

- [1] W. Zappa, M. Junginger, M. van den Broek, Is a 100% renewable european power system feasible by 2050?, *Applied Energy* 233-234 (2019) 1027 – 1050.
- [2] Y. Gao, J. Dong, O. Isabella, R. Santbergen, H. Tan, M. Zeman, G. Zhang, A photovoltaic window with sun-tracking shading elements towards maximum power generation and non-glare daylighting, *Applied Energy* 228 (2018) 1454 – 1472.
- [3] A. Elia, M. Kamidelivand, F. Rogan, B. Ó Gallachóir, Impacts of innovation on renewable energy technology cost reductions, *Renewable and Sustainable Energy Reviews* (2020) 110488.
- [4] K. Keeratimahat, A. Bruce, I. MacGill, Analysis of short-term operational forecast deviations and controllability of utility-scale photovoltaic plants, *Renewable Energy* (2020).
- [5] J.-S. Chou, N.-S. Truong, Cloud forecasting system for monitoring and alerting of energy use by home appliances, *Applied Energy* 249 (2019) 166 – 177.
- [6] A. Colmenar-Santos, A.-R. Linares-Mena, E.-L. Molina-Ibáñez, E. Rosales-Asensio, D. Borge-Diez, Technical challenges for the optimum penetration of grid-connected photovoltaic systems: Spain as a case study, *Renewable Energy* 145 (2020) 2296 – 2305.
- [7] J. Alonso-Montesinos, F. Batlles, The use of a sky camera for solar radiation estimation based on digital image processing, *Energy* 90 (2015) 377 – 386.
- [8] P. Tzoumanikas, E. Nikitidou, A. Bais, A. Kazantzidis, The effect of clouds on surface solar irradiance, based on data from an all-sky imaging system, *Renewable Energy* 95 (2016) 314 – 322.
- [9] D. Mateos, M. Antón, A. Valenzuela, A. Cazorla, F. Olmo, L. Alados-Arboledas, Efficiency of clouds on shortwave radiation using experimental data, *Applied Energy* 113 (2014) 1216 – 1219.
- [10] J. S. Bartlett, Á. M. Ciotti, R. F. Davis, J. J. Cullen, The spectral effects of clouds on solar irradiance, *Journal of Geophysical Research: Oceans* 103 (C13) (1998) 31017–31031.

- [11] X. Chen, Y. Du, E. Lim, H. Wen, K. Yan, J. Kirtley, Power ramp-rates of utility-scale pv systems under passing clouds: Module-level emulation with cloud shadow modeling, *Applied Energy* 268 (2020) 114980.
- [12] M. Diagne, M. David, P. Lauret, J. Boland, N. Schmutz, Review of solar irradiance forecasting methods and a proposition for small-scale insular grids, *Renewable and Sustainable Energy Reviews* 27 (Supplement C) (2013) 65 – 76.
- [13] C. Voyant, G. Notton, S. Kalogirou, M.-L. Nivet, C. Paoli, F. Motte, A. Fouilloy, Machine learning methods for solar radiation forecasting: A review, *Renewable Energy* 105 (Supplement C) (2017) 569 – 582.
- [14] D. Yang, J. Kleissl, C. A. Gueymard, H. T. Pedro, C. F. Coimbra, History and trends in solar irradiance and pv power forecasting: A preliminary assessment and review using text mining, *Solar Energy* 168 (2018) 60–101.
- [15] H. T. Pedro, C. F. Coimbra, Assessment of forecasting techniques for solar power production with no exogenous inputs, *Solar Energy* 86 (7) (2012) 2017 – 2028.
- [16] M. Gohari, B. Urquhart, H. Yang, B. Kurtz, D. Nguyen, C. Chow, M. Ghonima, J. Kleissl, Comparison of solar power output forecasting performance of the total sky imager and the university of california, san diego sky imager, *Energy Procedia* 49 (2014) 2340 – 2350, proceedings of the SolarPACES 2013 International Conference.
- [17] N. Lindsay, Q. Libois, J. Badosa, A. Migan-Dubois, V. Bourdin, Errors in pv power modelling due to the lack of spectral and angular details of solar irradiance inputs, *Solar Energy* 197 (2020) 266 – 278.
- [18] O. Perpiñán, E. Lorenzo, Analysis and synthesis of the variability of irradiance and pv power time series with the wavelet transform, *Solar Energy* 85 (1) (2011) 188 – 197.
- [19] M. David, F. H. R. Andriamasomanana, O. Liandrat, Spatial and temporal variability of pv output in an insular grid: Case of reunion island, *Energy Procedia* 57 (2014) 1275–1282.
- [20] K. Lappalainen, S. Valkealahti, Output power variation of different pv array configurations during irradiance transitions caused by moving clouds, *Applied Energy* 190 (2017) 902 – 910.
- [21] M. Khashei, M. Bijari, An artificial neural network (p, d, q) model for timeseries forecasting, *Expert Systems with applications* 37 (1) (2010) 479–489.
- [22] S. Makridakis, E. Spiliotis, V. Assimakopoulos, Statistical and machine learning forecasting methods: Concerns and ways forward, *PloS one* 13 (3) (2018) e0194889.

- [23] N. Engerer, F. Mills, Kpv: A clear-sky index for photovoltaics, *Solar Energy* 105 (2014) 679 – 693.
- [24] C. J. Smith, J. M. Bright, R. Crook, Cloud cover effect of clear-sky index distributions and differences between human and automatic cloud observations, *Solar Energy* 144 (2017) 10–21.
- [25] A. Murata, H. Ohtake, T. Oozeki, Modeling of uncertainty of solar irradiance forecasts on numerical weather predictions with the estimation of multiple confidence intervals, *Renewable Energy* 117 (2018) 193 – 201.
- [26] O. García-Hinde, G. Terrén-Serrano, M. Hombrados-Herrera, V. Gómez-Verdejo, S. Jiménez-Fernández, C. Casanova-Mateo, J. Sanz-Justo, M. Martínez-Ramón, S. Salcedo-Sanz, Evaluation of dimensionality reduction methods applied to numerical weather models for solar radiation forecasting, *Engineering Applications of Artificial Intelligence* 69 (2018) 157 – 167.
- [27] R. Perez, S. Kivalov, J. Schlemmer, K. H. Jr., D. Renné, T. E. Hoff, Validation of short and medium term operational solar radiation forecasts in the us, *Solar Energy* (2010).
- [28] H. Escrig, F. Batlles, J. Alonso, F. Baena, J. Bosch, I. Salbidegoitia, J. Burgaleta, Cloud detection, classification and motion estimation using geostationary satellite imagery for cloud cover forecast, *Energy* 55 (Supplement C) (2013) 853 – 859.
- [29] C. Arbizu-Barrena, J. A. Ruiz-Arias, F. J. Rodríguez-Benítez, D. Pozo-Vázquez, J. Tovar-Pescador, Short-term solar radiation forecasting by advecting and diffusing msg cloud index, *Solar Energy* 155 (Supplement C) (2017) 1092 – 1103.
- [30] H. S. Jang, K. Y. Bae, H. S. Park, D. K. Sung, Solar power prediction based on satellite images and support vector machine, *IEEE Transactions on Sustainable Energy* (2016).
- [31] M. Šinko, P. Sýkora, P. Kamencay, R. Hudec, Development of a system for collecting and processing sky images and meteorological data used for weather prediction, *Transportation Research Procedia* 40 (2019) 1548 – 1554, tRANSCOM 2019 13th International Scientific Conference on Sustainable, Modern and Safe Transport.
- [32] M. Caldas, R. Alonso-Suárez, Very short-term solar irradiance forecast using all-sky imaging and real-time irradiance measurements, *Renewable Energy* 143 (2019) 1643 – 1658.
- [33] H.-Y. Cheng, C.-L. Lin, Cloud detection in all-sky images via multi-scale neighborhood features and multiple supervised learning techniques, *Atmospheric Measurement Techniques* 10 (1) (2017) 199–208.

- [34] C.-L. Fu, H.-Y. Cheng, Predicting solar irradiance with all-sky image features via regression, *Solar Energy* 97 (2013) 537 – 550.
- [35] C. Shi, Y. Zhou, B. Qiu, J. He, M. Ding, S. Wei, Diurnal and nocturnal cloud segmentation of all-sky imager (asi) images using enhancement fully convolutional networks, *Atmospheric Measurement Techniques* 12 (2019) 4713–4724.
- [36] A. Taravat, F. Del Frate, C. Cornaro, S. Vergari, Neural networks and support vector machine algorithms for automatic cloud classification of whole-sky ground-based images, *IEEE Geoscience and Remote Sensing Letters* 12 (02 2015).
- [37] A. Mammoli, A. Ellis, A. Menicucci, S. Willard, T. Caudell, J. Simmins, Low-cost solar micro-forecasts for pv smoothing, in: 2013 1st IEEE Conference on Technologies for Sustainability (SusTech), 2013, pp. 238–243.
- [38] W. Kong, Y. Jia, Z. Y. Dong, K. Meng, S. Chai, Hybrid approaches based on deep whole-sky-image learning to photovoltaic generation forecasting, *Applied Energy* 280 (2020) 115875.
- [39] A. Mammoli, G. Terrén-Serrano, A. Menicucci, T. P. Caudell, M. Martínez-Ramón, An experimental method to merge far-field images from multiple longwave infrared sensors for short-term solar forecasting, *Solar Energy* 187 (2019) 254–260.
- [40] J. Alonso, F. Batlles, G. López, A. Ternero, Sky camera imagery processing based on a sky classification using radiometric data, *Energy* 68 (2014) 599 – 608.
- [41] J. A. Shaw, P. W. Nugent, N. J. Pust, B. Thurairajah, K. Mizutani, Radiometric cloud imaging with an uncooled microbolometer thermal infrared camera, *Opt. Express* 13 (15) (2005) 5807–5817.
- [42] J. A. Shaw, P. W. Nugent, Physics principles in radiometric infrared imaging of clouds in the atmosphere, *European Journal of Physics* 34 (6) (2013) S111–S121.
- [43] B. Thurairajah, J. A. Shaw, Cloud statistics measured with the infrared cloud imager (ici), *IEEE Transactions on Geoscience and Remote Sensing* 43 (9) (2005) 2000–2007.
- [44] P. W. Nugent, J. A. Shaw, S. Piazzolla, Infrared cloud imaging in support of earth-space optical communication, *Opt. Express* 17 (10) (2009) 7862–7872.
- [45] N. J. P. Paul W. Nugent, Joseph A. Shaw, Correcting for focal-plane-array temperature dependence in microbolometer infrared cameras lacking thermal stabilization, *Optical Engineering* 52 (6) (2013) 1 – 8 – 8.

- [46] R. Chauvin, J. Nou, S. Thil, A. Traoré, S. Grieu, Cloud detection methodology based on a sky-imaging system, *Energy Procedia* (2015).
- [47] H.-Y. Cheng, Cloud tracking using clusters of feature points for accurate solar irradiance nowcasting, *Renewable Energy* 104 (2017) 281 – 289.
- [48] Y. Chu, M. Li, C. F. Coimbra, Sun-tracking imaging system for intra-hour dni forecasts, *Renewable Energy* 96 (2016) 792 – 799.
- [49] M. Hasenbalg, P. Kuhn, S. Wilbert, B. Nouri, A. Kazantzidis, Benchmarking of six cloud segmentation algorithms for ground-based all-sky imagers, *Solar Energy* 201 (2020) 596 – 614.
- [50] G. Terrén-Serrano, M. Martínez-Ramón, Comparative analysis of methods for cloud segmentation in infrared images (2020). [arXiv:2012.06930](#).
- [51] B. K. Horn, B. G. Schunck, Determining optical flow, *Artificial intelligence* 17 (1-3) (1981) 185–203.
- [52] B. D. Lucas, T. Kanade, An iterative image registration technique with an application to stereo vision (1981).
- [53] G. Farnebäck, Two-frame motion estimation based on polynomial expansion, *Image analysis* (2003) 363–370.
- [54] P. Shaffery, A. Habte, M. Netto, A. Andreas, V. Krishnan, Automated construction of clear-sky dictionary from all-sky imager data, *Solar Energy* 212 (2020) 73 – 83.
- [55] L. Adrian, R. Adrian, J. Westerweel, *Particle Image Velocimetry*, Cambridge Aerospace Series, Cambridge University Press, 2011.
- [56] G. Terrén-Serrano, M. Martínez-Ramón, Data acquisition and image processing for solar irradiance forecast (2020). [arXiv:2011.12401](#).
- [57] P. Kuhn, S. Wilbert, C. Prah, D. Schüler, T. Haase, T. Hirsch, M. Wittmann, L. Ramirez, L. Zarzalejo, A. Meyer, et al., Shadow camera system for the generation of solar irradiance maps, *Solar Energy* 157 (2017) 157–170.
- [58] G. Masters, W. online library, *Renewable and Efficient Electric Power Systems*, Wiley - IEEE Series, Wiley, 2004.
- [59] J. Nocedal, S. J. Wright, *Numerical Optimization*, 2nd Edition, Springer, New York, NY, USA, 2006.
- [60] D. Lamb, J. Verlinde, *Physics and Chemistry of Clouds*, Cambridge University Press, 2011.

- [61] A. N. Tikhonov, V. Y. Arsenin, Solutions of ill-posed problems, V. H. Winston & Sons, Washington, D.C.: John Wiley & Sons, New York, 1977, translated from the Russian, Preface by translation editor Fritz John, Scripta Series in Mathematics.
- [62] H. C. Andrews, C. L. Patterson, Digital interpolation of discrete images, IEEE Transactions on Computers C-25 (2) (1976) 196–202.
- [63] G. Terrén-Serrano, M. Martínez-Ramón, Multi-layer wind velocity field visualization in infrared images of clouds (2020). [arXiv:2012.02861](#).
- [64] S. Baker, R. Gross, T. Ishikawa, I. Matthews, Lucas-kanade 20 years on: A unifying framework: Part 2, International Journal of Computer Vision 56 (2003) 221–255.
- [65] R.-E. Fan, K.-W. Chang, C.-J. Hsieh, X.-R. Wang, C.-J. Lin, Liblinear: A library for large linear classification, J. Mach. Learn. Res. 9 (2008) 1871–1874.
- [66] C. wei Hsu, C. chung Chang, C. jen Lin, A practical guide to support vector classification (2010).
- [67] L. L. Pan, L. A. Munchak, Relationship of cloud top to the tropopause and jet structure from calipso data, Journal of Geophysical Research: Atmospheres 116 (D12) (2011).
- [68] J. Hummel, W. Kuhn, Comparison of radiative-convective models with constant and pressure-dependent lapse rates, Tellus 33 (3) (1981) 254–261.